CrystEngComm

Accepted Manuscript

ROYAL SOCIETY OF CHEMISTRY

www.rsc.org/crystengcomm

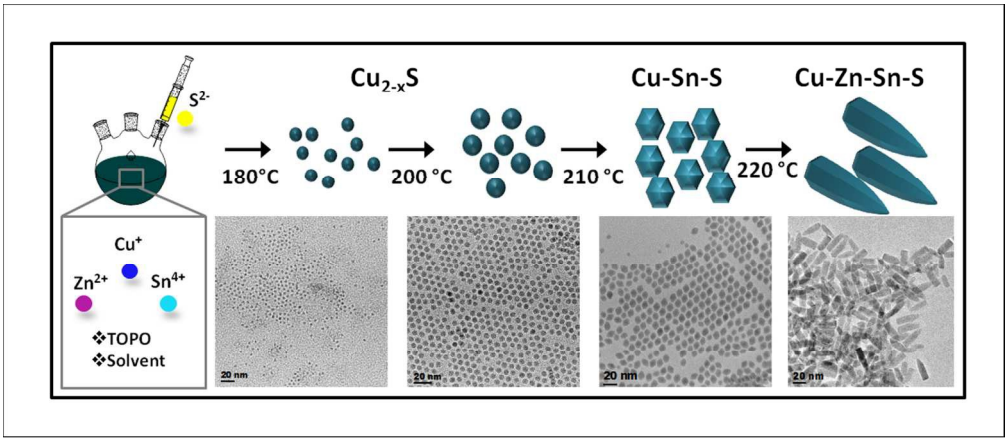

208x90mm (150 x 150 DPI)

Journal Name

RSCPublishing

ARTICLE

Complete Study of the Composition and Shape Evolution in the Synthesis of Cu_2ZnSnS_4 (CZTS) Semiconductor Nanocrystals

Cite this: DOI: 10.1039/x0xx00000x

Received 00th January 2012,
Accepted 00th January 2012

DOI: 10.1039/x0xx00000x

www.rsc.org/

Claudia Coughlan,[a] and Kevin M. Ryan*[a]

This article describes a complete study of the evolution of composition (from binary to quaternary) and shape (0D-1D) during the synthesis of CZTS nanocrystals. Aliquot studies were used to track the nucleation and growth in the early stages. Distinctive stages are evident in the reaction due to the progressive incorporation of tin and zinc into the primary copper sulfide particles as a result of their differing precursor reactivity. In addition, reaction windows for shape control were devised by tuning the amine concentration, thereby allowing the formation of a diverse range of shape morphologies including nanorods and ellipsoids, as well as atypical tadpole-shaped and P-shaped nanocrystals. Polytypic nanocrystals with wurtzite and zinc blende domains were also achieved by changing the type of metal precursors used initially in the reaction.

Introduction

Colloidal nanocrystal routes to fabricate a range of copper-based semiconductors, namely $CuInS_2$ (CIS), $CuInSe_2$ (CISe), $CuInGaS_2$ (CIGS) and Cu_2ZnSnS_4 (CZTS), have recently attracted a great deal of attention.[1-14] These materials are potential alternatives to cadmium and lead chalcogenides for photoconversion and photoemission applications, having high optical absorption coefficients and band-gaps that are tunable according to composition.[9, 12, 14-19] The most successful colloidal nanocrystal synthetic platform uses a hot-injection approach typically of an anion complex into a melted surfactant mixture containing the cation precursors.[3, 7, 9, 15, 20-22] The instantaneous supersaturation from the injection allows the concentration to rapidly supercede the nucleation threshold, with simultaneous growth of all particles equally. As the compositions progress from binary to quaternary, control of the reactions requires balancing the chemical potentials of the increasing number of different metal cations, in addition to the cation and surfactant species.[1, 15, 23, 24] The occurrence and control of polymorphism is a further interesting challenge in these systems. Stabilization of the metastable wurtzite phase for example is attractive as the random cation distribution (of Zn/Sn ions) offers flexibility for stoichiometry control and ultimately the ability to tune the Fermi energy over a wide range.[3, 14, 25] It also allows for the formation of rod-shaped nanocrystals, in which elongation occurs along the unique c-axis of the hexagonal crystal lattice,[3, 9, 26-28] serving to enhance total absorption and directional charge transfer.[22, 29-33]

The co-existence of two crystal phases in a single nanocrystal (referred to as polytypism) is also possible and is a phenomenon that has already been widely observed in tetrahedrally coordinated semiconductors, most notably in II-VI nanostructures as a result of their large atom stacking freedom.[34, 35] Zinc blende (ZB) and wurtzite (WZ) modifications possess relatively low energy differentials, thus switching between these polymorphs is possible kinetically through temperature modulation or by selective ligand attachment.[34] Previous reports of Cu-based polytypic nanocrystals have been observed, particularly in relation to $Cu_2ZnSn(SSe)_4$ (CZTSSe)[36] and $Cu_2CdSn(SSe)_4$ (CCTSSe)[37] nanocrystals where linearly arranged polytypic nanocrystals with rugby ball-like and bullet-like morphologies were formed, respectively. More recently, our group synthesized Cu_2SnSe_3 (CTSe) tetrapods[38] and linear polytypic heterostructures[39] while the work of Zamani et al and Cabot et al reported the formation of $Cu_2Cd_xSnSe_y$ (CCTSe) polypods[40] and Cu_2GeSe_3 (CGSe) nanoparticles,[41] respectively.

Of all the copper-chalcogenides formed, CZTS in particular is attractive as all the elements are highly earth abundant, thereby offering a sustainable material candidate for photovoltaics.[22, 42-48] CZTS nanocrystals have been predominantly formed in the kesterite structure and we recently demonstrated the formation of nanorods by using a hot-injection approach to nucleate in the wurtzite phase, with subsequent growth along the [001] direction.[22] These rods could subsequently be assembled into highly ordered thin film absorber layers. The potential for even finer shape control was evident in this work, with rods either forming as a conventional cylinder or a more faceted bullet shape depending on the subtle variations of

ligand/precursor combinations. A full study of crystal phase and shape control in the colloidal CZTS nanocrystal system has not been carried out and is of considerable interest as it would allow particle design to the facet level for optimisation for the desired technological application. Achieving this requires a detailed understanding of CZTS nanocrystal formation through the nucleation and growth stages and understanding and control of the critical factors that influence the morphology.

In this work, we carry out a complete study of shape control in the CZTS nanocrystal system. Aliquot studies are used to track the nucleation and growth in the early stages as particles initially form as binary copper sulfide before the progressive incorporation of zinc and tin. After the desired composition is reached, the subsequent growth of the particle allows for reaction windows for shape control whereby solely varying the concentration of amine solvent in the reaction, we observe the formation of nanorods and ellipsoids, as well as atypical tadpole-shaped and P-shaped nanocrystals. Furthermore, we show how changing the precursors used for the synthesis, specifically the copper and zinc precursor, influences the reaction environment and allows the evolution of multi-phase polytypic CZTS nanocrystals with wurtzite and zinc blende domains. Two distinctive CZTS morphologies, namely acorn-shaped and pencil-shaped nanocrystals, were obtained representing the first observation of polytypism in this system. Through HRTEM imaging, XRD and FFT analysis, the polytypic nanocrystals were observed to be comprised of well-defined zinc blende and wurtzite crystal frameworks in separate domains of the same crystal, with high resolution measurements allowing clear visualization of their differing atom stacking arrangements.

Results and Discussion

To gain important insights into the evolution pathway of the CZTS reaction to form wurtzite nanorods, aliquots were withdrawn from the reaction mixture at desired intervals in the growth zone (after nucleation – injection of the anion precursor). Fig. 1 summarizes the TEM analysis of aliquots taken at 10° temperature increments from the reaction mixture, ranging from 180°C to 220°C and the associated solution colour changes as a result of the increasing temperature and growth time. Additional low and high resolution TEM images are provided in Fig. S1. Fig. 1a presents a schematic of the hot-injection colloidal approach employed to achieve CZTS nanocrystals. The cationic and anionic precursors are separated up until the point of injection as demonstrated in Fig. 1a, in which the reaction flask contains the metal cationic precursors (Cu, Zn, Sn) dissolved in a surfactant (TOPO) and solvent (ODE) mixture, before the injection of the anionic chalcogen (thiol mixture comprised of t-DDT and 1-DDT) at 155°C. Although aliquots were also withdrawn from the flask at 160°C and 170°C, it was difficult to obtain nanocrystals (after the centrifugation process) in these aliquots, most likely due to the extremely small size of the crystallites formed in the initial stages. TEM analysis of the aliquot taken at 180°C and 4.5 minutes after the thiol injection (Fig. 1b) reveals the presence of tiny (<2 nm) particles at this point, with high resolution imaging of individual nanocrystals proving difficult. At 190°C and 6.5 minutes after injection, the resultant nanocrystals (Fig. 1c) are pseudo spherical in shape and are approximately 3.6nm ± 0.6nm in diameter. These nanocrystals undergo an increase in size to 6nm ± 1nm at 200°C (Fig. 1d-i) with an orange-brown solution colour apparent (inset of Figure 1d-i). This colour change is consistent with the formation of $Cu_{2-x}S$ nanocrystals in the reaction, in agreement with our previous observations in the CIGS system.[7]

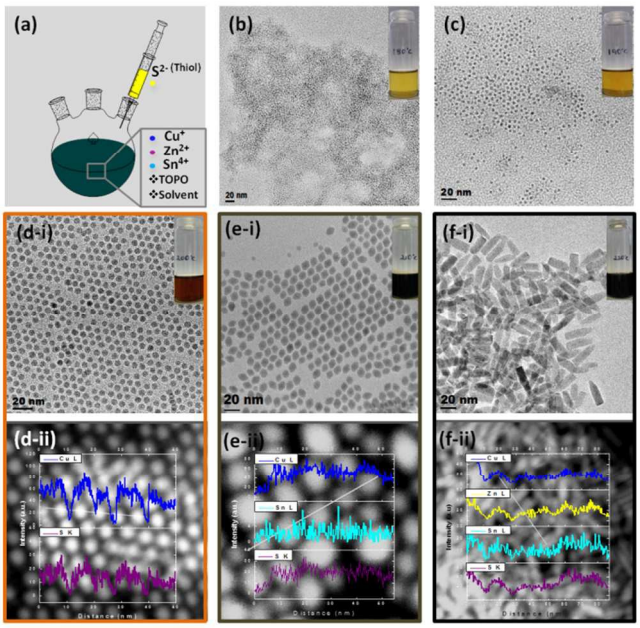

Fig. 1 (a) Schematic of the hot injection approach to form CZTS nanorods. (b-f) TEM Analysis of aliquots removed from the reaction flask at 10°C increments after injection of the thiol mixture, specifically at (b) 180°C, (c) 190°C, (d) 200°C, (e) 210°C and (f) 220°C. Photographs of the corresponding vials containing aliquots taken at each of the specified temperatures are shown in the inset of each TEM image. DF-STEM and EDX line scan analysis of aliquots taken at (g) 200°C, (h) 210°C and (i) 220°C.

Dark field scanning transmission electron microscopy (DF-STEM) and elemental line scan analysis of this sample at 200°C (across the measured line as depicted in Fig. 1d-ii) reveals that the nanocrystals are composed of only two elements at this stage, specifically Cu and S and were devoid of Zn and Sn ions despite their presence in solution. At 210°C, a morphological change is observed in the nanocrystals (Fig. 1e-i), changing from spherical to rhombus-shaped nanocrystals, with measured dimensions of 12.5nm ± 1.5 nm in length and 10 ± 1nm in diameter at the widest point. EDX analysis of this sample (Fig. 1e-ii) detects the presence of minor quantities of tin in the nanocrystals, thus signalling the onset of tin incorporation into the nanocrystals at 210°C. At 220°C, another change in the morphology is observed, with the resultant nanorods possessing a bullet shape on the terminating growth facets (Fig. 1f-i). The corresponding EDX elemental analysis (Fig. 1f-ii) revealed the presence of equal quantities of both zinc and tin in the nanorods, thus forming the stoichiometric composition of CZTS. These observations clearly identify the region between 200°C and 220°C as crucial in the formation of CZTS nanorods, with both tin and zinc incorporating into the pre-formed $Cu_{2-x}S$ nuclei, respectively, and within a short timeframe in this narrow temperature range. Further low resolution DF-STEM images of aliquots taken from 200°C-220°C are shown in Fig. S2.

Based on the compilation of TEM and EDX observations of aliquots withdrawn from the reaction, the proposed growth mechanism for CZTS nanorods can be devised. Fig. 2 shows a schematic illustration summarizing the observations made from both measurements and the temperature ramp applied during the synthesis, complete with a

colour profile of the associated solution colour changes as a result of the increasing reaction temperature.

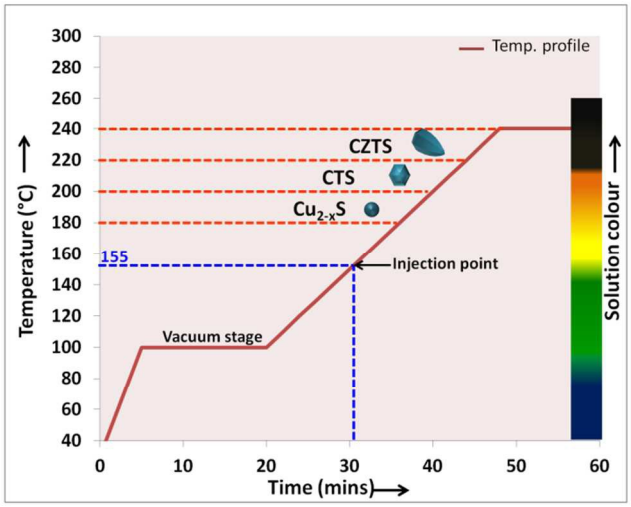

Fig. 2 Schematic illustration of the proposed growth mechanism for CZTS nanocrystals divided into different windows to document the evolution pathway during the temperature ramp. An accurate representation of the solution colour changes as a result of the increasing temperature is also shown.

Before injection of the thiol mixture, the reaction mixture changes from dark blue to a turbid dark green solution (beyond 90°C) due to the thermal decomposition of the $Cu(acac)_2$ precursor. Immediately after injection of the thiol mixture at 155°C, the solution turns bright yellow as a result of the high concentration of sulfur precursor and its reaction with the $Cu(acac)_2$ precursor, thus leading to the formation of a copper thiolate [$Cu(SC_{12}H_{25})$] intermediate within seconds after injection. The formation of this intermediate correlates well with previous observations in the binary Cu_2S nanocrystal system.[49] The increasing reaction temperature accelerates the decomposition of [$Cu(SC_{12}H_{25})$], with the consequent colour transition from yellow to orange signalling an accumulation of active monomer species and leading to the formation of nuclei upon supersaturation. At 180°C, particles (< 2nm) were already apparent in the reaction (see Fig. 1b) and were encased in a gel-like polymeric substance, attributed to unreacted [$Cu(SC_{12}H_{25})$]. After the formation of the initial nuclei, the remaining monomer species adds onto the surface of the $Cu_{2-x}S$ nuclei, with the increasing temperature promoting nanocrystal growth as confirmed by an increasing particle size from 3.6nm (190°C, Fig. 1c) to 6nm (200°C, Fig. 1d-i). Similar observations for the formation of $Cu_{2-x}S$ nuclei in the early stages of ternary and quaternary copper chalcogenides have been previously reported.[3, 7, 50-56] The differences in the reactivity of the metal precursors result in several windows in the evolution pathway as shown in Fig. 2, starting with the formation of $Cu_{2-x}S$ nuclei (180-200°C), followed by the diffusion of Sn^{4+} into the pre-formed nuclei to form Cu-Sn-S bonds(CTS, 200-210°C) , before the final Zn^{2+} incorporation yielding Cu_2-Zn-Sn-S_4 (CZTS, 220-240°C). This transformation is also accompanied with a change in the morphology, starting from a pseudo spherical shape through a rhombus-like morphology before the final evolution to CZTS nanorods.

Once CZTS is formed, there is a reaction window for shape control that can be tuned by the amine concentration present initially in the reaction flask. Fig. 3(a-c) shows the formation of highly monodisperse CZTS nanorods, synthesized with up scaled quantities as per Singh et al's report[22] when no amine is present in the reaction flask (i.e. synthetic route R1, using 1-octadecene (ODE) as the sole solvent).

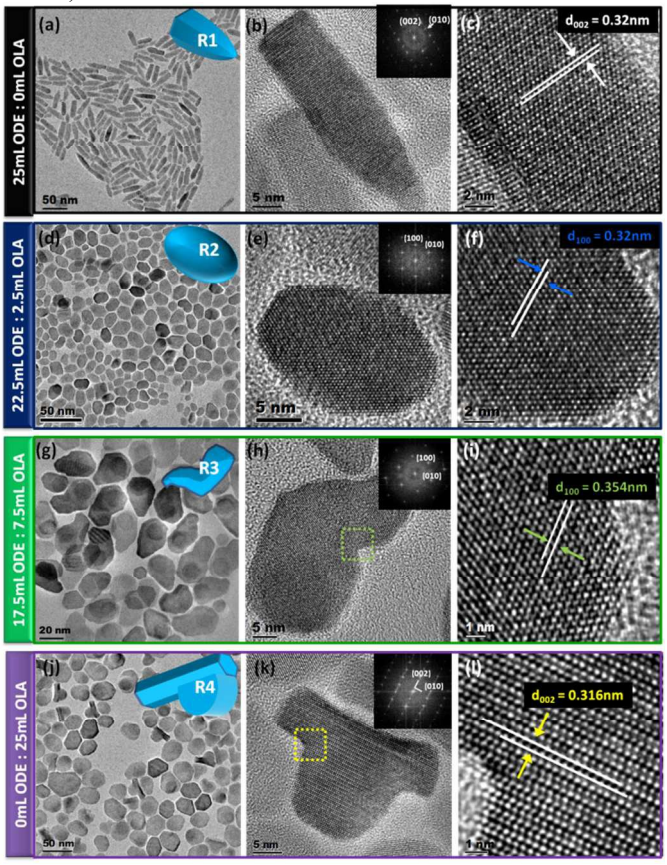

Fig. 3 TEM images of the diverse CZTS morphologies obtained through modulation of the oleylamine (OLA) concentration, with each morphology imaged under low and high resolution. (a-c) Bullet shaped nanorods formed in route R_1 using ODE as sole solvent, with the inset FFT image in (b) viewed along the [100] direction. (d-f) Ellipsoid shaped nanocrystals formed in route R_2, with the inset FFT image in (e) viewed along the [001] direction. (g-i) Tadpole shaped nanocrystals formed in route R_3 with an increased OLA content. The inset FFT image in (h) is viewed along the [001] direction. (j-l) P-shaped nanocrystals formed in R_4 using OLA as sole solvent, with the inset in (k) viewed along the [100] direction.

The as-synthesized nanorods possess a high degree of shape and size control, as shown in Fig. 3a, with the nanorods having an average length of 38 ± 2 nm and diameter of 11 ± 0.6 nm. HRTEM analysis of an individual nanorod (Fig. 3b) reveals that the nanorods are highly crystalline, with a predominant bullet shape on the terminating end facets. The measured angle of 90.5° (measured from inset FFT pattern, Fig. 3b) correlates with the theoretical angle (90°) between the (002) and (010) planes in a hexagonal crystal system. From the magnified view in Fig. 3c, a d-spacing of 0.32nm was measured in the nanorod and shows good agreement with the (002) plane of the wurtzite structure.

When a mixed solvent system comprised of 22.5mL ODE and 2.5mL OLA is used, significant changes in the morphology of the resultant nanocrystals occur, with the evolution of ellipsoid shaped nanocrystals as shown in Fig. 3(d-f). From the low resolution TEM image in Fig. 3d, and HRTEM Fig. 3e relatively narrow size distributions of ellipsoid shaped

nanocrystals were formed, having dimensions of 18nm ± 1.5 nm in length and 12 ± 2.5 nm in diameter. The increased diameter in the ellipsoid morphology, as opposed to nanorods, infers that OLA preferentially binds to the (002) nanocrystal facet in this system. While OLA causes clear changes in the nanocrystal shape, its effects are solely limited to morphological control and its presence does not exert phase control in this reaction, evidenced by the attainment of exclusively the wurtzite structure in these nanocrystals. This is depicted in Fig. 3f, where the atom stacking arrangement (AB/AB for the wurtzite system) is visualized along the tip of the ellipsoid. The measured d-spacing of 0.32nm in this particular nanocrystal also matches well with the (100) plane of the wurtzite phase.

Further increases in the concentration of OLA in the solvent mix (17.5mL ODE: 7.5mL OLA, route R3) significantly perturbed the reaction environment and lead to the formation of tadpole-shaped nanocrystals, as shown in Fig. 3g. These unusual nanocrystals were approximately 32.5 ± 4 nm in length and 25 ±2.1 nm in diameter across the top section. Upon closer inspection, slight morphological variations of the tadpole-shape are formed in this reaction as a result of capturing the nanocrystals at different stages in their growth e.g. Fig. 3g. These shape perturbations do not result in any change in the phase, with HRTEM measurements (Fig. 3h,i) confirming the wurtzite structure. Tadpole shaped nanostructures have also been previously reported in different copper chalcogenide systems, specifically in $CuGaS_2$ (CGS)[9, 57] and $CuInGaS_2$ (CIGS) nanocrystals.[7, 9] Based on our observations, the increased proportion of amine in the ODE : OLA solvent combination most likely raises the energy of the (002) face and leads to the exposure of the lower-energy crystal faces. This results in growth progressing along the (100) faces (as evidenced by the HRTEM image in Fig. 3h) to minimize the surface area of the high energy (002) face. Similar phenomena have been observed previously in the II-VI nanocrystals[27, 35] and more recently in the I-III-$V1_2$ nanocrystal system when the system was perturbed by excess OLA or hexadecylamine (HDA).[7]

Complete replacement of the ODE solvent with OLA (i.e. 0mL ODE :25mL OLA, route R4) also affected the shape during the synthesis, leading to P-shaped nanocrystals as shown in Fig. 3(j- *l*). Higher degrees of polydispersity are noted in reactions dominated by OLA solvent and so, P-shaped nanocrystals are not exclusively formed e.g. Fig. 3j. A closer look at the P-shaped nanocrystals reveals that they consist of a hemisphere-like segment located on top of an elongated nanocrystal. A higher magnification TEM image of an individual nanocrystal is shown in Fig. 3k, with the inset FFT pattern indexed to the (002) and (010) planes oriented at 90° angles. Fig. 3*l* shows a magnified view of the region highlighted in Fig. 3k, revealing the atom stacking arrangement (AB/AB stacking), complete with a measured d_{002} spacing of 0.316nm. P-shaped nanocrystals of CIS have been previously observed by Kruszynska et al, with the addition of TOPO (a hard Lewis base and coordinating solvent) decreasing and regulating the activity of the indium precursor (a hard Lewis acid) in their system.[3] Herein, we hypothesize that the substantial increased concentration of OLA (another well known coordinating solvent) in the reaction environment causes rapid decomposition of the cationic precursors, leaving only a small amount of precursors behind for the second growth stage. The unreacted precursors left behind in this reaction consequently result in continued growth of the nuclei, forming large and irregular shaped nanocrystals, principally distinctive P-shaped nanocrystals in this specific synthetic route (R_4). Similar observations in relation to OLA expediting the precursor decomposition process have also been previously reported in copper based chalcogenide nanocrystals.[3, 14, 17, 58, 59]

XRD measurements were conducted on each of the diverse morphologies, ranging from the conventional nanorod geometry (R_1) to ellipsoids (R_2), tadpole-shaped (R_3) and P-shaped nanocrystals (R_4). The resultant XRD pattern for the nanocrystals obtained in each route is shown in Fig. 4. Each pattern displays strong reflections attributed to the (100), (002), (101), (102), (110), (103), (112) planes constituting the hexagonal system of CZTS. Since no standard XRD pattern exists in the database for the hexagonal structured CZTS system, a simulated pattern was obtained based on the lattice parameters, as calculated from the experimental XRD pattern (CZTS_R1 in Fig. 4). Both the experimental and simulated patterns match well for each morphology, confirming the wurtzite structure of the nanocrystals. Furthermore, the lattice parameters (a=b=3.8076Å and c=6.2749Å) agree well with those reported previously.[50, 53, 60] Additional details on the pattern simulation is provided in the Supporting Information, as summarized in Table S1 and Table S2. EDX analysis of each morphology (Fig. S3) confirmed the presence of all 4 elements (Cu,Zn,Sn,S) and more importantly, that stoichiometric variations did not exist despite the differences in nanocrystal shape.

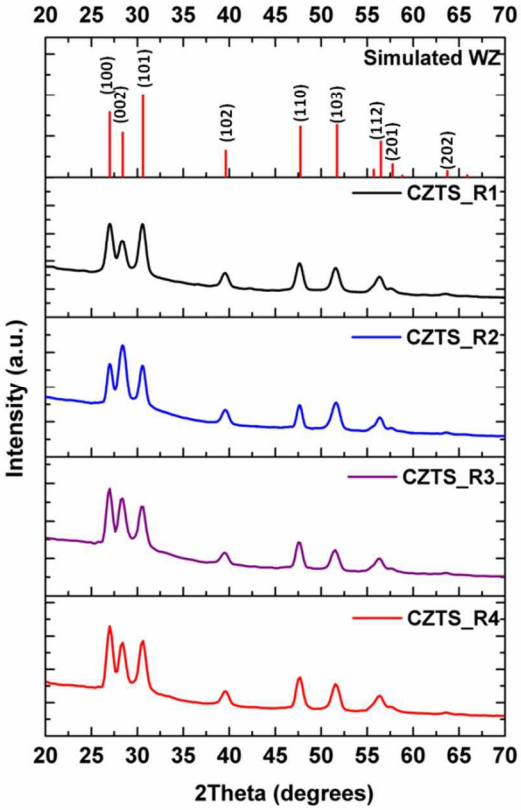

Fig. 4 XRD patterns of the different CZTS morphologies synthesized in routes R1-R4, specifically nanorods (R1), ellipsoid-shaped nanocrystals (R2), tadpole-shaped nanocrystals (R3) and P-shaped nanocrystals (R4), complete with the simulated XRD pattern of the wurtzite (WZ) structure for comparison.

While synthetic routes R_1-R_4 involved modulation of the OLA concentration in the ODE:OLA solvent mixture, each route afforded the formation of a differently shaped nanocrystal crystallizing with a single phase, hexagonal wurtzite structure. Interestingly, a change in the metal precursors (specifically utilizing cationic precursors containing chloride counter ions) resulted in the formation of multi-phase or polytypic nanocrystals in this system, adopting acorn-like and pencil-like morphologies.

By selecting OLA as the reaction solvent and replacing the copper (II) acetylacetonate precursor, $Cu(acac)_2$, with copper(I) chloride (CuCl), acorn-like polytypic nanorods were achieved in route R_5, as shown in Fig. 5a. The HRTEM image in Fig. 5b reveals much finer details on their exact morphology. The nanocrystals have dimensions of 30.8 ± 1.8 nm in length and 20.5 ± 1 nm in diameter and consist of a wide bullet-like shape,with a smaller abrupt hemisphere-like section at one side of the bullet. This gives rise to their so-called acorn-like morphology.

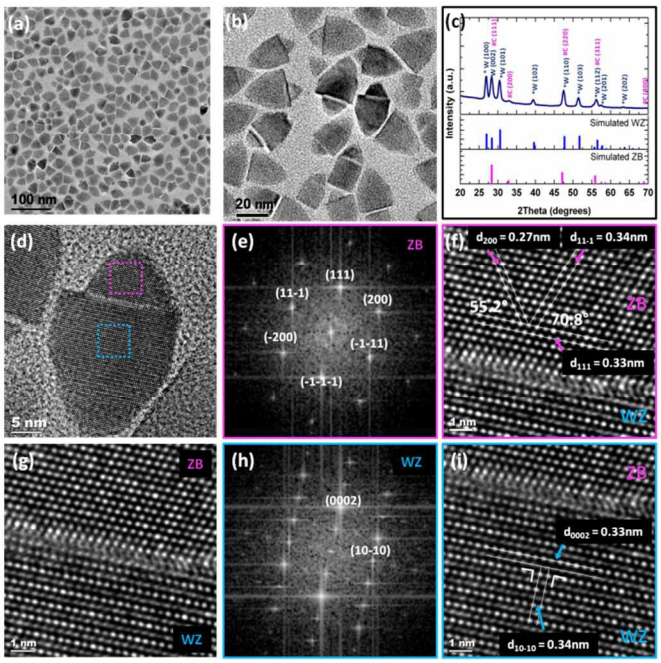

Fig. 5 Polytypic CZTS Nanocrystals with Acorn-like morphology synthesized in R_5. (a) Low resolution TEM image of the as-synthesized nanocrystals. (b) Higher magnification TEM image aiding in identifying their morphology. (c) XRD pattern of the as-synthesized nanocrystals. (d) HRTEM image of an individual polytypic nanocrystal, with the simulated patterns of wurtzite (WZ) and zinc-blende (ZB) provided for reference. (e) FFT pattern of the narrow segment constituting the zinc-blende crystal domain. (f) Magnified HRTEM image of the zinc blende domain. (g) HRTEM image of the interface between the separate domains. (h) FFT pattern of the wider segment of the acorn-shaped nanocrystal comprising the wurtzite domain. (i) Magnified HRTEM image of the wurtzite domain.

Their crystalline structure was further characterized by XRD, as depicted in Fig. 5c, with the main peaks indexed to the (100), (002), (101), (102), (110), (103), (112) planes of the wurtzite structure. The increased intensity of the (002), (100) and (112) peaks, coupled with the appearance of peaks at 33.0° and 63.4°2θ (characteristic of the (200) and (400) planes in a cubic lattice), further confirms the presence of an additional cubic phase in these nanocrystals. The aforementioned stronger intensity of the (002), (100) and (112) planes, indexed to the wurtzite structure, occurs as a result of peak overlap of the (111), (220) and (311) planes in the zinc blende phase. As one can see in Fig. 5c, the experimental pattern matches well with the simulated diffraction patterns of both the wurtzite phase and zinc blende phase of CZTS. These simulated patterns were obtained through calculation of the lattice parameters and assignment of the space group for each phase. In particular, the lattice parameters were calculated to be a = b = 3.8076Å and c = 6.2749Å for the wurtzite phase, with the simulation based on a hexagonal structured lattice with $P6_3mc$ (no.186) space group. For the zinc-blende phase, the lattice parameters were determined to be a = b = c = 5.4507Å and the pattern was simulated having a cubic structured lattice with F -43 m (no.216) space group.

A HRTEM image of an individual polytypic nanocrystal is shown in Fig. 5d, allowing identification of well defined zinc blende and wurtzite crystal frameworks in separate regions of the same crystal. In particular, the smaller segment of the acorn shape was observed to crystallize in the cubic zinc blende (ZB) phase and the wider bullet-like segment of the acorn was comprised of hexagonal wurtzite (WZ) phase. The co-existence of these two domains (both WZ and ZB) can be achieved in these nanocrystals due to the equivalence of the (002) atomic planes of the hexagonal structure with the (111) atomic planes of the cubic structure. The corresponding FFT pattern (Fig. 5e) of the smaller segment of the acorn shape is fully indexed to the cubic crystal structure. From the magnified HRTEM image of the ZB domain in Fig. 5f, interplanar spacings of 0.33nm, 0.27nm and 0.34nm were directly measured and were indexed to the (111), (200) and (11-1) planes of the ZB structure, respectively. The angles between these observed planes were also determined, as shown in Fig. 5f, and were calculated to be 55.2° (between the (111) and (200) planes) and 70.8° (between the (111) and (11-1) planes), which shows good agreement with the theoretical values of 55° and 71° for these planes in a cubic structured crystal. Fig. 5g shows a magnified HRTEM image of the interface of the ZB and WZ derived structures where the lattice mismatch is evident. The ZB derived structure possesses a well defined anion stacking sequence of ABC/ABC (viewed along the [111] direction), in contrast to the AB/AB stacking sequence in the WZ structure (viewed along the [0001] direction). The corresponding FFT pattern (depicted in Fig. 5h) and the magnified HRTEM image (Fig. 5i) of the WZ section revealed d-spacings of 0.34nm and 0.33nm, indexed to the (0002) and (10-10) planes of the WZ structure.

Of the copper based organometallic precursors, copper chloride (CuCl) displays the fastest reactivity due to its soft acid (Cu^+) and hard base (Cl^-) assignments in the hard-soft acid-base (HSAB) theory and this infers that a weak binding interaction (increased precursor reactivity) exists in CuCl. We hypothesize that this increased precursor reactivity, coupled with the use of OLA as solvent, results in an expedited precursor decomposition process that significantly affects nanocrystal nucleation and growth. This ultimately tunes the chemical environment and allows for the co-existence of ZB and WZ derived structures in separate domains of the same crystal. In a separate report, Wang et al also discovered that the use of metal chlorides as cation precursors provided optimal control in the formation of tetrapod and linear heterostructures comprised of Cu_2SnSe_3 (CTSe).[38, 39] In order to fully assess and understand how and when the polytypic structure forms in the CZTS system, an aliquot study was conducted by withdrawing samples from the reaction flask as growth proceeded (Fig. S4). Importantly, the results revealed that spherical nanocrystals form in the initial stages after injection and up to 200°C (consistent with observations in Fig. 1b-d), before transitioning

through a single-phase ellipsoidal morphology at 220°C. At 230°C, the early onset of polytypic nanocrystal growth was observed to occur, in which small segments of the ZB phase nucleate and grow off the main WZ body of the nanocrystals. This reveals that growth of the ZB phase is principally driven by the elevated reaction temperature, particularly once the temperature exceeds 230°C in this system, with its nucleation and growth from the main WZ body consistent with the heterogeneous growth model.

Another linearly arranged, polytypic morphology was also attained in this system as shown in Fig. 6.

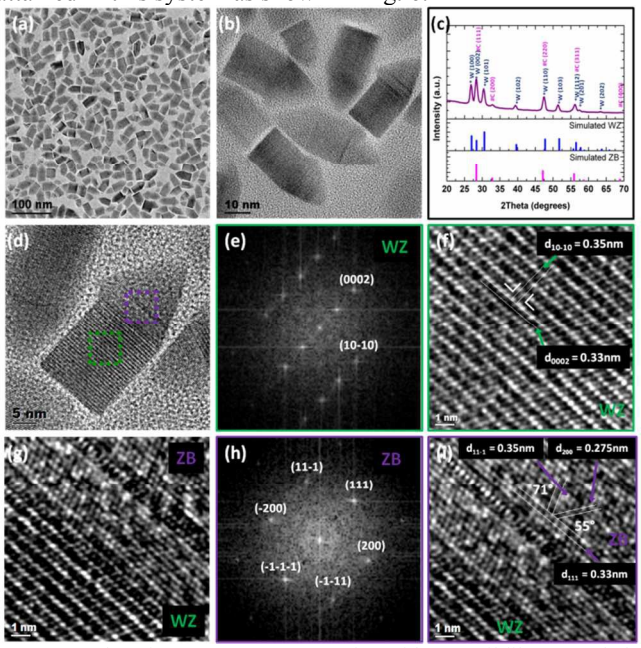

Fig. 6 Polytypic CZTS Nanocrystals with Pencil-like morphology synthesized in R_6. (a) Low resolution TEM image. (b) Higher magnification TEM image revealing finer morphological details. (c) XRD pattern of the as-synthesized nanocrystals, with the simulated WZ and ZB patterns provided for reference. (d) HRTEM image of an individual polytypic nanocrystal. (e) FFT pattern of the central segment comprised of the WZ structure (f) Magnified HRTEM image of the WZ domain. (g) HRTEM image of the interface between the separate domains. (h) FFT pattern of the tip segment of the pencil-shaped nanocrystal composed of the ZB structure. (i) Magnified HRTEM image of the ZB domain, complete with angular measurements between the identified planes.

While synthetic route R_5 involved the selection of CuCl and zinc acetate ($Zn(Ac)_2$), as copper and zinc precursors respectively, we observed that the further replacement of $Zn(Ac)_2$ with the $Zn(Cl)_2$ precursor resulted in the formation of pencil-like CZTS polytypic nanocrystals (Fig. 6a,b) having dimensions of 34 ± 2 nm in length and 17.5 ± 1.5 nm in diameter. XRD analysis (Fig. 6c) indicates that the nanocrystals are composed of both WZ and ZB phases, as confirmed by comparison of the experimental XRD pattern with that of the simulated patterns, and also by FFT and lattice fringing measurements of each segment (Fig. 6d-i).

The direct observation of a vast range of shape variations by solely manipulating the ODE: OLA solvent ratio shows that the nature of the solvent plays a key role in influencing the CZTS nanocrystal morphology. Further manipulation of the metal precursor choice shows that small variations in reactivity of the species present can induce polytypism where two crystal phases can exist in an individual nanocrystal.

Conclusions

In summary, we have investigated the evolution pathway of CZTS nanocrystals revealing that copper sulfide nanoparticles form in the early stages of the reaction before the progressive incorporation of tin and zinc to form stoichiometric CZTS. This occurs concomitantly with a shape change in the particle from 0D to 1D, with growth along the [001] direction. In addition, reaction windows for shape control are available, whereby modulation of the amine concentration present initially in the reaction allows for the evolution of atypical morphologies, namely ellipsoid, tadpole and P-shaped nanocrystals. The inherent reactivity of the metal precursors, specifically the copper and zinc precursor, was also revealed to have an effect by providing optimal conditions to achieve multi-phase or polytypic nanocrystals. Replacement of the copper precursor, $Cu(acac)_2$, with CuCl, allows the formation of polytypic acorn-shaped nanocrystals whereas replacement of the zinc precursor, $ZnAc_2$ with $ZnCl_2$, resulted in pencil shaped nanocrystals. Both morphologies were revealed to be comprised of separate ZB and WZ domains. The ability to control shape and polytypism in CZTS nanocrystals is important as this allows for design of nanocrystals for particular applications. For photovoltaics, phase boundaries are often sites with prevalence for electron trapping and so, single phase nanocrystals (or complete suppression and elimination of polytypism) are optimal in this application, with maximization of length dependent properties such as total absorption and directional charge transfer being highly desirable. [22, 29-33] On the other hand, for thermoelectrics, the co-occurrence of two phases in single particles has been shown to be optimal[36, 40, 41], where multi-phase nanocrystals result in lower thermal conductivities and a higher thermoelectric figure of merit than comparable single phase nanocrystals. Thus, the ability to control multi-phase formation in colloidal CZTS nanocrystals through subtle changes in the reaction chemistry allows optimization for the desired end application.

Experimental Section

Materials

All reagents were used as received without any further purification. Copper(II) acetylacetonate ($Cu(acac)_2$; >99.99%), Copper(I)chloride (CuCl >99.99%), Zinc acetate ($Zn(Ac)_2$, >99.99%), Zinc (II) chloride ($ZnCl_2$>99.99%), Tin(IV) acetate ($Sn(Ac)_4$, >99.99%), Trioctylphosphine oxide (TOPO, 99%), 1-dodecanethiol (1-DDT, 98%), tert-dodecylmercaptan (t-DDT, 98.5%, mixture of isomers), 1-Octadecene (ODE, 90%, technical grade) and Oleylamine (OLA, technical grade, 70%) were purchased from Aldrich.

Synthesis of CZTS Nanorods (R_1):

In a typical synthesis of CZTS nanorods, $Cu(acac)_2$ (0.6545g, 2.5mmol), $Zn(Ac)_2$ (0.2292g, 1.25 mmol), $Sn(Ac)_4$ (0.4435g, 1.25mmol), TOPO (3.383g ,8.75 mmol) and 1-octadecene (25mL) were added to a three-neck, round-bottom flask, fitted with reflux condenser, rubber septum and temperature finger. The contents of the flask were evacuated at 100°C for 15mins to eliminate adventitious water and dissolved oxygen. The reaction mixture was then heated to 250°C (30°C /min) under an argon atmosphere and at 155°C, a 5mL thiol mixture (comprised of 4.375mL t-DDT and 0.625mL 1-DDT) was rapidly injected into the system. After injection, the reaction was allowed to proceed for 30minutes with

continuous stirring. Subsequently, the heating mantle was removed and the reaction vessel was allowed to cool to 80°C. 2-3mL of toluene was added initially to quench the reaction. The nanocrystals were then washed twice with a 1:2 ratio of toluene to iso-propanol (IPA) and centrifuged at 4000rpm for 7mins to yield the dark red centrifuged product. After each centrifugation, the supernatant was removed and the precipitated nanorods were re-dispersed in toluene for further characterization.

Synthesis of CZTS Nanocrystals with different morphologies (R_1-R_4)

A diverse range of CZTS morphologies were formed through variation of the 1-octadecene : oleylamine (ODE:OLA) solvent ratio, as outlined in table 1. All other synthetic parameters were kept constant, as per CZTS nanorod route (R1).

Synthesis Route #	ODE:OLA Solvent ratio (mL)	Resultant Morphology
R1	25.0 : 0 (100% : 0%)	Nanorod
R2	22.5 : 2.5 (90 : 10%)	Ellipsoid-shape
R3	17.5 : 7.5 (70% :30%)	Tadpole-shape
R4	0 : 25.0 (0% :100%)	P-shape

Table 1. Details of Synthetic Routes (R_1-R_4) identifying the ODE: OLA solvent ratio added to the flask in the initial step (also denoted as relative % content of each solvent for clarity).

Synthesis of Polytypic CZTS Nanocrystals with an Acorn-like morphology (R_5):

Polytypic CZTS nanocrystals with an acorn-like morphology were synthesized using the following protocol. CuCl (0.099g, 1mmol), $Zn(Ac)_2$ (0.0917g, 0.5 mmol), $Sn(Ac)_4$ (0.1774g, 0.5mmol), TOPO (1.3532g ,8.75 mmol) and oleylamine (25mL) were added to a three-neck round-bottom flask. The flask was evacuated at 100°C for 15mins and was then subsequently heated to 250°C (30°C /min) under an argon atmosphere. When the temperature reached 155°C, a 2mL thiol mixture (comprised of 1.75mL t-DDT and 0.25mL 1-DDT) was rapidly injected into the system. After injection, the reaction was allowed to proceed for 30minutes with continuous stirring. Subsequently, the heating mantle was removed and the reaction vessel was allowed to cool to 80°C. A similar washing procedure, as outlined in R_1, was conducted.

Synthesis of Polytypic CZTS Nanocrystals with Pencil-like morphology (R_6):

Polytypic CZTS nanocrystals with a pencil-like morphology were synthesized using an identical protocol to that as outlined in route R_5 except with the following exception: $Zn(Ac)_2$ precursor is replaced with $Zn(Cl)_2$ (0.068g, 0.5mmol).

Characterization

For transmission electron microscopy (TEM) analysis, 2mL aliquots of the reaction mixture were taken by syringe at specified times and quenched via cooling to room temperature. Nanocrystals were precipitated from the reaction mixture and dissolved in toluene. TEM samples were prepared on 200 mesh carbon-coated copper grids (Ted Pella Inc.). TEM and Dark-field scanning transmission electron microscopy (DFSTEM) was conducted by using a 200 kV JEOL JEM-2100F field emission microscope, equipped with a Gatan Ultrascan CCD camera and EDAX Genesis EDS detector. Samples for EDX were prepared on carbon-coated nickel TEM grids. X-ray diffraction (XRD) analysis of drop-cast films of CZTS nanocrystals on a glass substrate was conducted using a PANalytical X'Pert PRO MRD instrument with a Cu Kα radiation source (λ = 1.5418 Å) and a 1-D X'celerator strip detector.

Acknowledgements

This work was supported by Science Foundation Ireland (SFI) under the Principal Investigator Program under contract No. 11PI-1148.

Notes and references

[a] Materials and Surface Science Institute and Department of Chemical and Environmental Sciences, University of Limerick, Limerick, Ireland. *Corresponding Author: E-mail: Kevin.M.Ryan@ul.ie

Electronic Supplementary Information (ESI) available: [Additional low and high resolution TEM images and DF-STEM images of aliquots taken at desired intervals after the injection. EDX elemental analysis of the different CZTS shape morphologies through modulation of the amine concentration. TEM analysis of aliquots taken to monitor the formation of acorn-shaped polytypic nanocrystals, XRD pattern simulation for the WZ and ZB phases]. See DOI: 10.1039/b000000x/

1. H. Zhong, S. S. Lo, T. Mirkovic, Y. Li, Y. Ding, Y. Li and G. D. Scholes, *ACS Nano*, 2010, 4, 5253-5262.
2. M. G. Panthani, V. Akhavan, B. Goodfellow, J. P. Schmidtke, L. Dunn, A. Dodabalapur, P. F. Barbara and B. A. Korgel, *Journal of the American Chemical Society*, 2008, 130, 16770-16777.
3. M. Kruszynska, H. Borchert, J. r. Parisi and J. Kolny-Olesiak, *Journal of the American Chemical Society*, 2010, 132, 15976-15986.
4. Q. Guo, S. J. Kim, M. Kar, W. N. Shafarman, R. W. Birkmire, E. A. Stach, R. Agrawal and H. W. Hillhouse, *Nano Letters*, 2008, 8, 2982-2987.
5. J. Tang, S. Hinds, S. O. Kelley and E. H. Sargent, *Chemistry of Materials*, 2008, 20, 6906-6910.

6. J.-J. Wang, Y.-Q. Wang, F.-F. Cao, Y.-G. Guo and L.-J. Wan, *Journal of the American Chemical Society*, 2010, 132, 12218-12221.
7. C. Coughlan, A. Singh and K. M. Ryan, *Chemistry of Materials*, 2013, 25, 653-661.
8. Y.-H. A. Wang, C. Pan, N. Bao and A. Gupta, *Solid State Sciences*, 2009, 11, 1961-1964.
9. Y.-H. A. Wang, X. Zhang, N. Bao, B. Lin and A. Gupta, *Journal of the American Chemical Society*, 2011, 133, 11072-11075.
10. M. Ahmadi, S. S. Pramana, L. Xi, C. Boothroyd, Y. M. Lam and S. Mhaisalkar, *The Journal of Physical Chemistry C*, 2012, 116, 8202-8209.
11. Q. Guo, G. M. Ford, H. W. Hillhouse and R. Agrawal, *Nano Letters*, 2009, 9, 3060-3065.
12. A. Singh, S. Singh, S. Levcenko, T. Unold, F. Laffir and K. M. Ryan, *Angewandte Chemie International Edition*, 2013, 52, 9120-9124.
13. X. Lu, Z. Zhuang, Q. Peng and Y. Li, *Chemical Communications*, 2011, 47, 3141-3143.
14. D. Pan, L. An, Z. Sun, W. Hou, Y. Yang, Z. Yang and Y. Lu, *Journal of the American Chemical Society*, 2008, 130, 5620-5621.
15. D. Aldakov, A. Lefrancois and P. Reiss, *Journal of Materials Chemistry C*, 2013, 1, 3756-3776.
16. E. Dilena, Y. Xie, R. Brescia, M. Prato, L. Maserati, R. Krahne, A. Paolella, G. Bertoni, M. Povia, I. Moreels and L. Manna, *Chemistry of Materials*, 2013, 25, 3180-3187.
17. D. Pan, X. Wang, Z. H. Zhou, W. Chen, C. Xu and Y. Lu, *Chemistry of Materials*, 2009, 21, 2489-2493.
18. F.-J. Fan, L. Wu, M. Gong, G. Liu, Y.-X. Wang, S.-H. Yu, S. Chen, L.-W. Wang and X.-G. Gong, *ACS Nano*, 2013, 7, 1454-1463.
19. S. C. Riha, B. A. Parkinson and A. L. Prieto, *Journal of the American Chemical Society*, 2011, 133, 15272-15275.
20. H. Zhou, W.-C. Hsu, H.-S. Duan, B. Bob, W. Yang, T.-B. Song, C.-J. Hsu and Y. Yang, *Energy & Environmental Science*, 2013, 6, 2822-2838.
21. F.-J. Fan, L. Wu and S.-H. Yu, *Energy & Environmental Science*, 2014, 7, 190-208.
22. A. Singh, H. Geaney, F. Laffir and K. M. Ryan, *Journal of the American Chemical Society*, 2012, 134, 2910-2913.
23. R. Xie, M. Rutherford and X. Peng, *Journal of the American Chemical Society*, 2009, 131, 5691-5697.
24. A. Singh, C. Coughlan, D. J. Milliron and K. M. Ryan, *Chemistry of Materials*, 2015, 27, 1517-1523.
25. Y. Qi, Q. Liu, K. Tang, Z. Liang, Z. Ren and X. Liu, *The Journal of Physical Chemistry C*, 2009, 113, 3939-3944.
26. X. Peng, *Advanced Materials*, 2003, 15, 459-463.
27. X. Peng, L. Manna, W. Yang, J. Wickham, E. Scher, A. Kadavanich and A. P. Alivisatos, *Nature*, 2000, 404, 59-61.
28. Y. Yin and A. P. Alivisatos, *Nature*, 2005, 437, 664-670.
29. K. M. Ryan, S. Singh, P. Liu and A. Singh, *CrystEngComm*, 2014, 16, 9446-9454.
30. D. Kelly, A. Singh, C. A. Barrett, C. O'Sullivan, C. Coughlan, F. R. Laffir, C. O'Dwyer and K. M. Ryan, *Nanoscale*, 2011, 3, 4580-4583.
31. J. Hu, L.-s. Li, W. Yang, L. Manna, L.-w. Wang and A. P. Alivisatos, *Science*, 2001, 292, 2060-2063.
32. R. Krahne, G. Morello, A. Figuerola, C. George, S. Deka and L. Manna, *Physics Reports*, 2011, 501, 75-221.
33. A. Singh, C. Coughlan, F. Laffir and K. M. Ryan, *ACS Nano*, 2012, 6, 6977-6983
34. L. Manna, D. J. Milliron, A. Meisel, E. C. Scher and A. P. Alivisatos, *Nat Mater*, 2003, 2, 382-385.
35. L. Manna, E. C. Scher and A. P. Alivisatos, *Journal of the American Chemical Society*, 2000, 122, 12700-12706.
36. F.-J. Fan, L. Wu, M. Gong, S. Y. Chen, G. Y. Liu, H.-B. Yao, H.-W. Liang, Y.-X. Wang and S.-H. Yu, *Sci. Rep.*, 2012, 2.
37. L. Wu, F.-J. Fan, M. Gong, J. Ge and S.-H. Yu, *Nanoscale*, 2014, 6, 3418-3422.
38. J. Wang, A. Singh, P. Liu, S. Singh, C. Coughlan, Y. Guo and K. M. Ryan, *Journal of the American Chemical Society*, 2013, 135, 7835-7838.
39. J.-j. Wang, P. Liu, C. C. Seaton and K. M. Ryan, *Journal of the American Chemical Society*, 2014, 136, 7954-7960.
40. R. R. Zamani, M. Ibáñez, M. Luysberg, N. García-Castelló, L. Houben, J. D. Prades, V. Grillo, R. E. Dunin-Borkowski, J. R. Morante, A. Cabot and J. Arbiol, *ACS Nano*, 2014, 8, 2290-2301.
41. M. Ibáñez, R. Zamani, W. Li, D. Cadavid, S. Gorsse, N. A. Katcho, A. Shavel, A. M. López, J.

R. Morante, J. Arbiol and A. Cabot, *Chemistry of Materials*, 2012, 24, 4615-4622.
42. Q. Guo, G. M. Ford, W.-C. Yang, B. C. Walker, E. A. Stach, H. W. Hillhouse and R. Agrawal, *Journal of the American Chemical Society*, 2010, 132, 17384-17386.
43. Q. Guo, H. W. Hillhouse and R. Agrawal, *Journal of the American Chemical Society*, 2009, 131, 11672-11673.
44. S. C. Riha, B. A. Parkinson and A. L. Prieto, *Journal of the American Chemical Society*, 2009, 131, 12054-12055.
45. C. Steinhagen, M. G. Panthani, V. Akhavan, B. Goodfellow, B. Koo and B. A. Korgel, *Journal of the American Chemical Society*, 2009, 131, 12554-12555.
46. A. Shavel, D. Cadavid, M. Ibáñez, A. Carrete and A. Cabot, *Journal of the American Chemical Society*, 2012, 134, 1438-1441.
47. K. Ramasamy, M. A. Malik and P. O'Brien, *Chemical Communications*, 2012, 48, 5703-5714.
48. R. Mainz, A. Singh, S. Levcenko, M. Klaus, C. Genzel, K. Ryan and T. Unold, *Nature communications*, 2014, 5.
49. Y. Wang, Y. Hu, Q. Zhang, J. Ge, Z. Lu, Y. Hou and Y. Yin, *Inorganic Chemistry*, 2010, 49, 6601-6608.
50. J. M. R. Tan, Y. H. Lee, S. Pedireddy, T. Baikie, X. Y. Ling and L. H. Wong, *Journal of the American Chemical Society*, 2014, 136, 6684-6692.
51. M. D. Regulacio, C. Ye, S. H. Lim, M. Bosman, E. Ye, S. Chen, Q.-H. Xu and M.-Y. Han, *Chemistry – A European Journal*, 2012, 18, 3127-3131.
52. H.-C. Liao, M.-H. Jao, J.-J. Shyue, Y.-F. Chen and W.-F. Su, *Journal of Materials Chemistry A*, 2013, 1, 337-341.
53. M. Li, W.-H. Zhou, J. Guo, Y.-L. Zhou, Z.-L. Hou, J. Jiao, Z.-J. Zhou, Z.-L. Du and S.-X. Wu, *The Journal of Physical Chemistry C*, 2012, 116, 26507-26516.
54. S. T. Connor, C.-M. Hsu, B. D. Weil, S. Aloni and Y. Cui, *Journal of the American Chemical Society*, 2009, 131, 4962-4966.
55. X. Lu, Z. Zhuang, Q. Peng and Y. Li, *CrystEngComm*, 2011, 13, 4039-4045.
56. J. Li, M. Bloemen, J. Parisi and J. Kolny-Olesiak, *ACS Applied Materials & Interfaces*, 2014, 6, 20535-20543.
57. M. D. Regulacio, C. Ye, S. H. Lim, Y. Zheng, Q.-H. Xu and M.-Y. Han, *CrystEngComm*, 2013, 15, 5214-5217.
58. N. Bao, X. Qiu, Y.-H. A. Wang, Z. Zhou, X. Lu, C. A. Grimes and A. Gupta, *Chemical Communications*, 2011, 47, 9441-9443.
59. S. Mourdikoudis and L. M. Liz-Marzán, *Chemistry of Materials*, 2013, 25, 1465-1476.
60. X. Zhang, G. Guo, C. Ji, K. Huang, C. Zha, Y. Wang, L. Shen, A. Gupta and N. Bao, *Sci. Rep.*, 2014, 4.

Graphic TOC